Received: 7 October 2023 | Revised: 15 April 2024 | Accepted: 2 May 2024

DOI: 10.1002/mp.17239

RESEARCH ARTICLE

MEDICAL PHYSICS

Statistical image reconstruction with beam-hardening compensation for X-ray CT by a calibration step (2DIterBH)

Daniel Sanderson[1,2] | **Cristóbal Martinez**[1,2] | **Jeffrey A. Fessler**[3] | **Manuel Desco**[1,2,4,5] | **Mónica Abella**[1,2,4]

[1]Dept. Bioingeniería, Universidad Carlos III de Madrid, Spain

[2]Instituto de Investigación Sanitaria Gregorio Marañón, Madrid, Spain

[3]Electrical Engineering and Computer Science department, The University of Michigan, Ann Arbor, USA

[4]Centro Nacional de Investigaciones Cardiovasculares Carlos III (CNIC), Madrid, Spain

[5]Centro de investigación en red en salud mental (CIBERSAM), Madrid, Spain

Correspondence
Mónica Abella and Manuel Desco
Departamento de Bioingeniería, Universidad Carlos III de Madrid, Avda. de la Universidad 30, Leganes, Madrid 28911, Spain.
Email: mabella@ing.uc3m.es and desco@hggm.es

Funding information
Ministerio de Ciencia e Innovación, Agencia Estatal de Investigación, Grant/Award Numbers: AEI/10.13039/501100011033, PID2019-110369RB-I00, PID2021-128862OB-I00; ERDF A way of making Europe, Grant/Award Number: PDC2021-121656-I00; European Union 'NextGenerationEU'/PRTR; Instituto de Salud Carlos III, Grant/Award Numbers: PMPTA22/00121, PMPTA22/00118; European Union 'NextGenerationEU'/MRR; European Union's Horizon 2020 Research and Innovation Programme, Grant/Award Number: 801091

Abstract

Background: The beam-hardening effect due to the polychromatic nature of the X-ray spectra results in two main artifacts in CT images: cupping in homogeneous areas and dark bands between dense parts in heterogeneous samples. Post-processing methods have been proposed in the literature to compensate for these artifacts, but these methods may introduce additional noise in low-dose acquisitions. Iterative methods are an alternative to compensate noise and beam-hardening artifacts simultaneously. However, they usually rely on the knowledge of the spectrum or the selection of empirical parameters.

Purpose: We propose an iterative reconstruction method with beam hardening compensation for small animal scanners that is robust against low-dose acquisitions and that does not require knowledge of the spectrum, overcoming the limitations of current beam-hardening correction algorithms.

Methods: The proposed method includes an empirical characterization of the beam-hardening function based on a simple phantom in a polychromatic statistical reconstruction method. Evaluation was carried out on simulated data with different noise levels and step angles and on limited-view rodent data acquired with the ARGUS/CT system.

Results: Results in small animal studies showed a proper correction of the beam-hardening artifacts in the whole sample, independently of the quantity of bone present on each slice. The proposed approach also reduced noise in the low-dose acquisitions and reduced streaks in the limited-view acquisitions.

Conclusions: Using an empirical model for the beam-hardening effect, obtained through calibration, in an iterative reconstruction method enables a robust correction of beam-hardening artifacts in low-dose small animal studies independently of the bone distribution.

KEYWORDS
artifacts, beam hardening, CT, penalized-likelihood, polychromatic, streaks

Daniel Sanderson and Cristóbal Martinez are contributed equally to this study.

1 | INTRODUCTION

Mass attenuation coefficients of tissues typically decrease as energy increases. This dependence, together with the polychromatic nature of the spectra, causes a preferential absorption of low-energy photons, inducing an increase of the spectrum mean energy. This energy shift, known as beam hardening, leads to two well-known artifacts in uncorrected reconstructed images: cupping in homogeneous regions and dark bands between dense areas in heterogeneous regions.[1]

Several strategies have been proposed in the literature to compensate for this effect. The use of physical filters is an effective way to decrease the number of low-energy photons reaching the patient, but this strategy alone is not enough to get rid of the artifacts. The method implemented in most commercial CT scanners is the water-linearization, based on a characterization of the energy-dependency of water attenuation.[2,3] However, since it assumes the object to be homogeneous, it only corrects the cupping artifact. To correct both cupping and dark-band artifacts, Joseph et al.[4] addressed the correction of dark bands by proposing a method that includes the bone thickness in a second-order polynomial. The coefficients of this polynomial, which control the dark-band reduction, can be found analytically using the spectrum or empirically by visual inspection. Kyriakou et al.[5] and Schuller et al.[6] followed the same idea but extended the second-order polynomial to a combination of original and overcorrected images. The optimum coefficients of the combination were calculated by maximizing flatness,[5] which has been shown to not completely compensate for the dark bands[7], or by minimizing the entropy,[6] which leads to certain overcompensation of the dark bands in real studies. One important drawback of all the previous methods is that the optimum parameters depend on the bone distribution in the slice, thus hindering the possibility of finding a unique set of optimum coefficients for the whole volume. A more accurate estimation of the coefficients was performed in,[8,9] based on the epipolar consistency conditions. However, the resulting images showed a non-realistic texture in soft tissue and the authors were unsure about its performance in clinical CT.

We recently proposed a post-processing method (*2DCalBH*) based on the characterization of the energy-dependent attenuation of soft tissue and bone by means of a calibration procedure,[10] which showed a proper compensation of the dark bands in all cases together with a good recovery of the monochromatic values. However, the main limitation of this method, shared by most previous post-processing methods, is the need of a preliminary bone segmentation, which can be challenging in low-dose acquisitions.

Iterative reconstruction methods are a good alternative for low-dose studies. Yan et al. proposed a non-statistical method that iteratively computed the volume fraction of two known tissues[11] with the information of the spectrum and the attenuation coefficients of the tissues. To improve robustness to noise, De Man et al.[12] proposed a maximum-likelihood iterative algorithm that decomposed the linear attenuation coefficient into photoelectric and Compton scatter components. The weight of each component was constrained based on prior tissue assumptions. Following this line, Elbakri and Fessler[13] developed a statistical method based on Poisson distributions, modeling the object as composed of known tissues that had to be segmented. This model was improved in[14] by allowing pixels to contain mixtures and including the segmentation in the cost function where it is iteratively updated. However, all the previous methods need the knowledge of the spectrum to characterize the beam-hardening effect produced by soft tissue and bone. To eliminate the need for spectrum knowledge, we recently proposed a method[15] that analytically approximated the beam-hardening function of soft tissue and bone with the 1D beam-hardening function of the water plus two parameters that can be empirically tuned. However, similarly to Joseph et al., the optimum coefficients in all these methods depend on the distribution of bone, thus hindering the possibility of finding a unique set of optimum coefficients for the whole volume.

In this work, we substitute the analytical approximation of the beam-hardening function with the empirical estimation proposed in.[10] The algorithm iteratively minimizes the Poisson likelihood and uses ordered subsets to accelerate computation. Preliminary results were presented in an earlier conference[16] based on simulated data using an ideal calibration phantom made up of soft tissue and bone. The present work extends these experiments, proposing a realistic calibration phantom made up of equivalent materials. We evaluated the algorithm on simulated data under low-sampling and low-SNR conditions, and real data with two sparse-view rodent studies acquired with the CT subsystem of an ARGUS/CT (SEDECAL) scanner.[17]

2 | MATERIALS AND METHODS

The proposed method, *2DIterBH*, is based on the combination of the statistical reconstruction algorithm proposed in.[15] which we will refer to as *1DIterBH* in this work, with the beam hardening function model used in *2DCalBH*.[10] We summarize here the equations for completeness, indicating the changes in the original formulations. We model the sinogram measurements as independently distributed Poisson random variables[18] contaminated by extra background counts, primarily scatter:

$$Y_i \sim Poisson\left\{\int I_i(\varepsilon)e^{-\int_{L_i}\mu(\varepsilon)dl}d\varepsilon + r_i\right\}, i = 1, \ldots, N \quad (1)$$

where $\mu(\varepsilon)$ is the attenuation coefficient at each energy ε, the integral in the exponent is taken over the line L_i followed by the ray, $I_i(\varepsilon)$ is the incident intensity, the term r_i accounts for mean scatter and other background signals for the i-th ray and N is the number of rays.

We assume that the object is composed of only two substances, soft tissue and bone. Image segmentation is avoided by modeling the tissue fraction in each pixel as a function of the estimated density in that pixel.[14,15] The resulting model for the attenuation coefficient at voxel j is as follows:

$$\mu_j(\varepsilon) = \sum_{k=1}^{2} m_k(\varepsilon)\rho_j f_k^j(\rho_j) = \left(m_s(\varepsilon) f_s^j(\rho_j) + m_b(\varepsilon) f_b^j(\rho_j)\right)\rho_j \quad (2)$$

where tissue fraction functions, $f_s^j(\rho_j)$ and $f_b^j(\rho_j)$, are built following the displacement model in[14] that considers mixed pixels at the boundaries and m_s and m_b denote the mass attenuation coefficients of soft tissue and bone, respectively. The coefficients were obtained with a third-order polynomial fitting[15] using linear least-squares regression. This resulted in:

$$f_s = \begin{cases} 1 & 0.0 \le \rho \le 1.1 \\ -7.87 + 20.286\rho - 14.706\rho^2 + 3.268\rho^3 & 1.1 < \rho < 1.9 \\ 0 & 1.9 \le \rho \end{cases} \quad (3)$$

$$f_b = \begin{cases} 0.0 & 0 \le \rho \le 1.1 \\ 1 - f_s & 1.1 < \rho < 1.9 \\ 1 & 1.9 \le \rho \end{cases} \quad (4)$$

where density ρ has units in g/cm^3. Thresholds for soft tissue (1.1 g/cm^3) and bone (1.9 g/cm^3) were determined taking into account the values provided by the National Institute of Standard and Technology (NIST).[19] From the previous equation, we consider the contribution of each tissue type to the line integral along the i-th ray as:

$$t_s^i(\rho) = \sum_{j=1}^{p} a_{ij} f_s^j(\rho_j)\rho_j \quad (5)$$

$$t_b^i(\rho) = \sum_{j=1}^{p} a_{ij} f_b^j(\rho_j)\rho_j \quad (6)$$

where a_{ij} are the elements of the system matrix (having units in cm). With the assumption of the two-tissue model and Equations (5) and (6), we rewrite Equation (1) as:

$$\bar{Y}_i(\rho) = I_i e^{-F\left(t_s^i, t_b^i\right)} + r_i; \rightarrow I_i = \int I_{0_i}(\varepsilon)d\varepsilon \quad (7)$$

where $F(t_s, t_b)$ is the beam-hardening function, defined as

$$F(t_s, t_b) = -\log \int \frac{I(\varepsilon)}{I} e^{-m_s(\varepsilon)t_s - m_b(\varepsilon)t_b}\, d\varepsilon \quad (8)$$

where the dependence on ray i is dropped for simplicity.

A. Algorithm

We use the negative log-likelihood to estimate the density vector ρ, which for Equation (1) is given by

$$-L(\rho) = \sum_{i=1}^{N} h_i\left(F\left(t_s(\rho), t_b(\rho)\right)\right), \quad (9)$$

where

$$h_i(I) = -Y_i \log\left(I_i e^{-I} + r_i\right) + I_i e^{-I} + r_i. \quad (10)$$

For regularization, we added a 3D roughness penalty function with the convex edge-preserving Huber potential[20,21] to improve spatial resolution uniformity:

$$R(\rho) = \sum_{j=1}^{N_p} \frac{1}{2} \sum_{k \in N_j} w_{jk} \cdot \psi(\rho_j - \rho_k);$$

$$\psi(t) = \begin{cases} \dfrac{|t|^2}{\delta} & |t| \le \delta \\ \delta|t| - \dfrac{\delta}{2} & |t| > \delta \end{cases} \quad (11)$$

where N_j is a neighborhood of pixels near pixel j, $w_{jk} = w_{kj}$, ψ is the convex edge-preserving Huber potential, and δ a threshold to apply the blurring depending on the difference of the pixel and its neighbors.

The combination of the likelihood with the regularization results in a new cost function:

$$\Phi(\rho) = -L(\rho) + \beta R(\rho) \quad (12)$$

where the scalar parameter β controls the tradeoff between the data-fit and the penalty terms.

We derived an iterative algorithm based on separable quadratic surrogates[13,15] resulting in the following update:

$$\rho^{n+1} = \rho^n - D^{-1}\nabla\Phi(\rho^n) \quad (13)$$

where D is a diagonal matrix that influences the rate of convergence. Instead of designing D to ensure a monotonically decrease of the cost function, we choose the elements of D by using the following pre-computed

curvature[13]:

$$d_j = \alpha \left(m_s(\varepsilon_{eff}) + m_b(\varepsilon_{eff})\right)^2 \sum_{i=1}^{N} a_{ij} \left(\sum_j a_{ij} \right) Y_i \quad (14)$$

where α is a parameter to accelerate the convergence. Finally, we use an ordered subsets approximation of (13) to increase speed.[22]

B. Beam-hardening function

Using (8) to compute the beam-hardening function $F(t_s, t_b)$ would require knowledge of the spectrum that is often unavailable. Instead, we characterize it using a calibration step with a phantom composed of soft tissue- and bone-equivalent materials, as proposed in.[10] The independent variables used in *2DCalBH* were the traversed thickness of each tissue.[10] That approximation cannot be used in the proposed iterative method, the goal of which is to estimate the density map, as shown in Equation (13). For this reason, we use the mass thickness independent variables in the beamhardening function. The transformation into mass thicknesses, t_s and t_b, is done by adding an additional multiplication of each mask by the density of the material (Figure 1), extracted from NIST.

The acquired beam-hardening function was fit to a logarithm function so that it can be integrated into the algorithm:

$$F(t_s, t_b) = -\ln\left(a * e^{-(b*t_s+c*t_b)} + (1-a) * e^{-(d*t_s+e*t_b)}\right), \quad (15)$$

where a, b, c, d, and e are the fitting coefficients obtained by non-linear least-squares with the coefficients equally weighted.

We use the calibration phantom described in,[10] composed of one half-cylinder of soft-tissue equivalent material and one triangular prism with rounded corners of bone-equivalent material to have many combinations of mass thicknesses. Since the beam hardening effect depends on the source energy, it is necessary to calibrate $F(t_s, t_b)$ for every voltage used in the scanner.

2.1 | Evaluation methods

We simulated a polychromatic spectrum with 50 kVp and 2.5 mm aluminum filtration to mimic a preclinical X-ray source. Based on this source model, we generated a set of transmission polychromatic Poisson X-ray projections with parallel-beam geometry using the Michigan Image Reconstruction Toolbox (MIRT), available at https://github.com/JeffFessler/mirt. The detector was modeled as a simple photon counting device. The sinogram had 512 radial bins with 0.1 mm ray spacing, covering 180 degrees. We simulated three scenarios depending on the number of projections and counts per detector element, as shown in Table 1. We did not simulate scatter.

TABLE 1 Dose scenarios.

Scenario	Number of projections	Counts per detector element
Standard-dose	180	10^6
Low-dose	180	10^5
Ultra-low-dose	60	10^5

We reconstructed the data using uncorrected Filtered Back-projection (*FBP*), *FBP+JS*,[4] *FBP+2DCalBH*,[10] a penalized weighted least-squares method (*PWLS*),[21] the polyenergetic algorithm proposed in[14] (that we call *SegFreePoly* in the rest of the document), *1DIterBH*[15] and the proposed polyenergetic method, *2DIterBH*.

Parameters for the *JS* method and *1DIterBH* were heuristically searched as those that visually reduced the dark bands, resulting in $A_{JS} = 1.44$ and $B_{JS} = 0.26$ cm^2/g and $A_{1DIterBH} = 3$ and $B_{1DIterBH} = 0.06$ cm^2/g, respectively. The polychromatic model in *SegFreePoly* was the same X-ray spectrum used for simulation (ideal case). The iterative algorithms ran 40 iterations and 12 subsets and $\beta = 0.1$ and $\delta = 0.005$ g/cm^3 for the standard-dose scenario and $\beta = 0.4$ and $\delta = 0.005$ g/cm^3 for the low-dose and ultra-low-dose scenarios. The parameter α was set to 0.1.

We then used a synthetic phantom composed of an ellipse of soft tissue (1.06 g/cm^3) with a major axis of 6 cm and a minor axis of 4.8 cm, one ellipsoid of fat (0.9 g/cm^3), and disks of bone (1.92 g/cm^3) with diameters from 0.62 cm to 0.32 cm to simulate standard- and ultra-low-dose acquisitions (see Table 1). We quantified the bias as the root mean square error (RMSE) relative to the reference image (image with the true density values) in the regions of interest of soft tissue, adipose tissue, and bone.

Finally, we used two rodent studies (head and abdominal), acquired with the CT subsystem of an ARGUS/CT (SEDECAL) scanner, a cone-beam micro-CT scanner based on a flat-panel detector.[17] We obtained 180 views covering 360 degrees with 50 kVp and 1 mm aluminum filtration. A 3D version of these algorithms was implemented substituting the MIRT-CPU kernels with the GPU-accelerated kernels from FUX-Sim.[23] Reconstructed volumes had a size of 514×514×574 voxels (0.121 mm^3 voxel size). Experiments were carried out in accordance with the Animal Experimentation Ethics Committee of the Community of Madrid (Ref. PROEX 332/15), following the EU Directive 2010/63EU and Recommendation 2007/526/EC, and the enforcement in Spain from the Real Decreto 53/2013.

All iterative methods were run with 20 iterations and 12 subsets on a computer with an Intel Core i7-8700 CPU, 32 GB of RAM, and an NVIDIA GeForce RTX2060. Run time of *PWLS*, *SegFreePoly* and *2DIterBH* was 73, 164, and 156 seconds per slice, respectively.

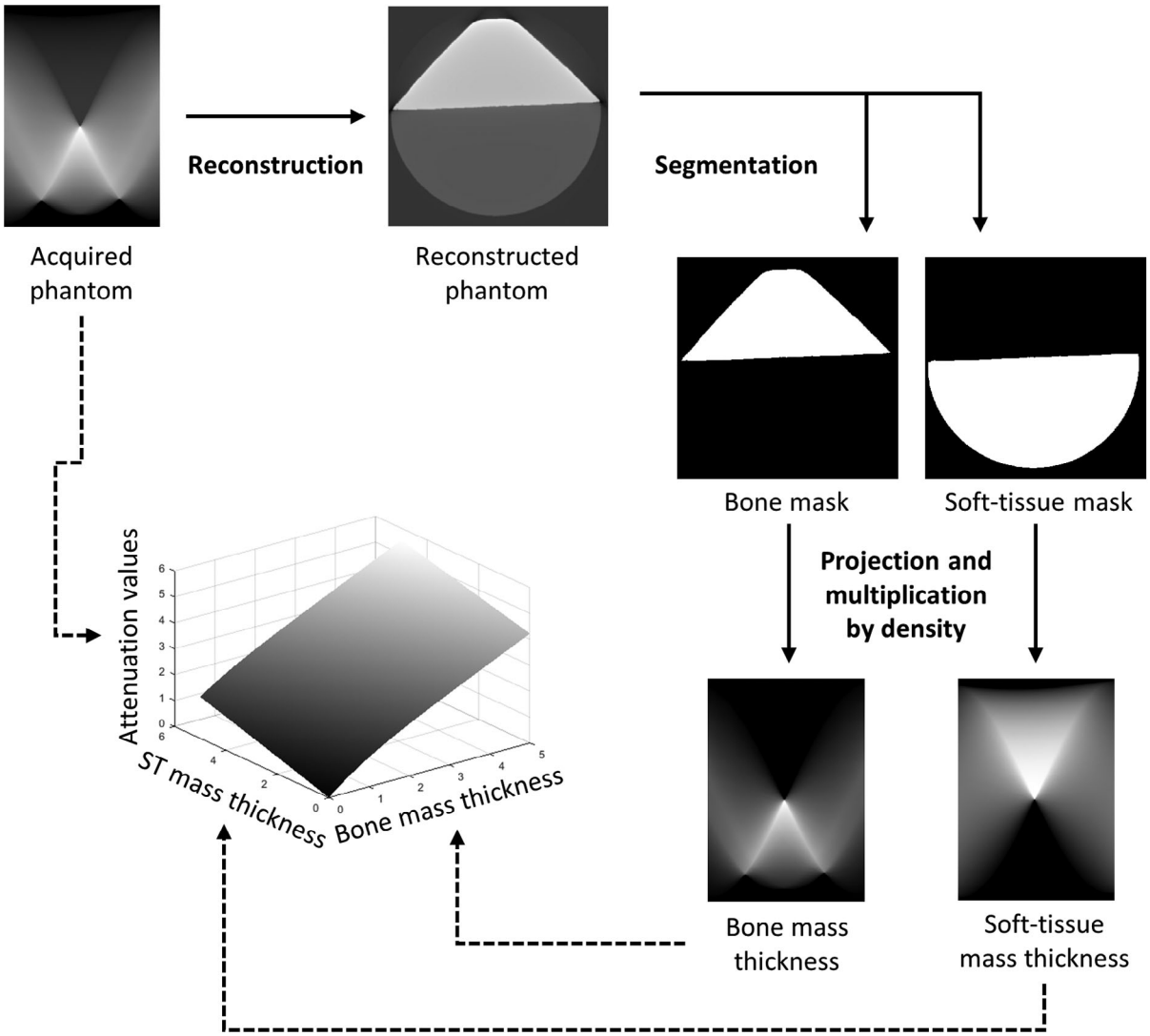

FIGURE 1 Workflow of the beam-hardening function characterization.

Regularization parameters, in this case, were $\beta = 10$ and $\delta = 0.01$ g/cm^3 for the head study and $\beta = 20$ and $\delta = 0.01$ g/cm^3 for the abdomen study, in all the iterative methods. Since the spectrum of the real system was not known, the polychromatic model in *SegFreePoly* was approximated by a simulated spectrum with the same kVp and Al filter. Parameters of *JS* and *1DIterBH* were selected heuristically as those that visually reduced the dark bands, as was done for the simulated data. Since it was impossible to find a set of parameters that result in an optimum correction for the whole volume, we considered from here on the slice with the most conspicuous dark bands as the "calibration slice". The values of these *JS* parameters were $A_{JS} = 0.1$ and $B_{JS} = 0.73$ cm^2/g and *1DIterBH* parameters were $A_{1DIterBH} = 2.458$ and $B_{1DIterBH} = 0.49$ cm^2/g. The parameter α was set to 0.5.

The calibration step used a calibration phantom made up of a semi-circle of equivalent soft tissue material (radius of 3 cm) and a rounded triangle of bone equivalent material (6 cm of width and 2.5 cm of height), as described in.[10] We used ideal soft tissue and bone for simulated data and PMMA and the aluminum alloy AL6082 both for simulated and real data as equivalent materials to soft tissue and bone[24] (Figure 2). R-square of the fitting in Equation (15) was greater than 0.99 for all cases.

3 | RESULTS

Figure 3 and Table 2 show the results with the synthetic phantom in the standard-dose scenario. As expected, the *FBP+JS* and the *FBP+2DCalBH* methods achieved a correction of the dark bands similar to that of the iterative methods *SegFreePoly*,*1DIterBH* and *2DIterBH*, while *PWLS* did not correct them. *SegFreePoly*, *1DIterBH* and *2DIterBH* methods obtained the lowest errors for all tissues. RMSE values for adipose tissue were higher than those for soft tissue in all methods.

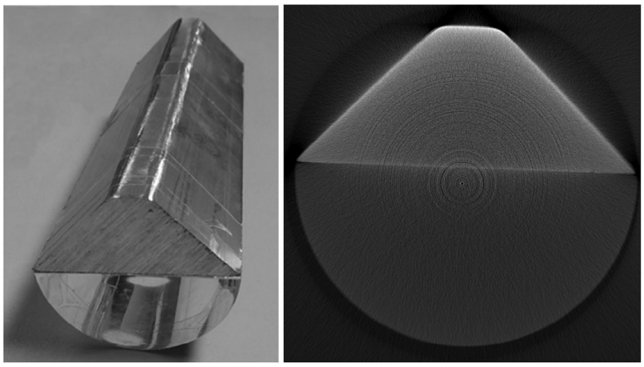

FIGURE 2 Calibration phantom composed of PMMA and AL6082 (left) and axial slice of the FDK reconstruction (right).

TABLE 2 Root mean square error (RMSE) results (g/cm^3) of the phantom under high-dose scenario.

Method	RMSE in soft tissue	RMSE in adipose tissue	RMSE in bone
FBP	0.14	0.18	2.66
FBP + JS	0.16	0.17	5.00
FBP + 2DCalBH	0.13	0.18	3.68
PWLS	0.11	0.17	0.24
SegFreePoly	0.07	0.15	0.04
1DIterBH	0.06	0.14	0.04
2DIterBH (ST-Bone)	0.06	0.14	0.04
2DIterBH (PMMA-AL6082)	0.10	0.02	0.08

TABLE 3 Root mean square error (RMSE) results (g/cm^3) of the phantom under ultra-low-dose scenario.

Method	RMSE in soft tissue	RMSE in adipose tissue	RMSE in bone
FBP	0.24	0.26	2.67
FBP + JS	0.34	0.34	4.86
FBP + 2DCalBH	0.27	0.30	3.71
PWLS	0.11	0.17	2.77
SegFreePoly	0.07	0.15	0,04
1DIterBH	0.06	0.14	0.05
2DIterBH (ST-Bone)	0.06	0.13	0.04
2DIterBH (PMMA-AL6082)	0.10	0.03	0.09

Using a realistic calibration phantom increased the error in soft tissue and bone with respect to the use of the ideal phantom but reduced it in adipose tissue. Note that errors in bone density for the three *FBP*-based methods were much higher due to the fact that *FBP* does not reconstruct density values.

Figure 4 and Table 3 show the results of the synthetic phantom in the ultra-low-dose scenario. *FBP+JS* and *FBP+2DCalBH* corrected the dark-bands artifacts but, as expected, highly increased the low-sampling artifacts, thus resulting in higher errors in soft tissue than in the standard-dose scenario. All iterative methods reduced these low-sampling artifacts with a similar result in the correction of dark bands and RMSE values.

Figure 5 shows the result of the head and abdomen rodent studies for the calibration slice (representative of nearby slices with similar bone distributions). The post-processing methods *FDK+JS* and *FDK+2DCalBH* corrected the dark bands but increased the low-sampling artifacts. *SegFreePoly* reduced the low sampling artifacts, but did not fully compensate the dark bands, showing that the ideal spectrum is not a good approximation in real studies. In contrast, *1DIterBH* and *2DIterBH* corrected both artifacts, low-sampling streaks and dark bands. In slices with a bone distribution different from that of the calibration slice, *FDK+JS* and *1DIterBH* did not completely correct the dark bands, while *FDK+2DCalBH* and *2DIterBH* corrected the dark bands in the whole sample, independently of the bone distribution (see Figure 6).

4 | DISCUSSION AND CONCLUSIONS

This work presents a new statistical reconstruction algorithm for polyenergetic CT that includes the estimation of the beam-hardening function based on calibration, described in,[10] in the statistical reconstruction method for polyenergetic X-ray CT proposed in.[15] The method enables a robust correction of both cupping and dark bands while reducing the noise and low-sampling artifacts present in low-dose acquisitions, and eliminating the need for prior knowledge of the spectrum[14] or empirical parameters[15] required by iterative reconstruction methods previously proposed in the literature.

No effort was done to optimize the algorithms. Better initialization obtained with *2DCalBH* could reduce the number of iterations required and runtime could be reduced on parallelized GPU nodes. To further reduce the computational time certain steps of the method could be replaced by deep-learning kernels, such as the soft thresholding segmentation or the regularization term. Using pure deep-learning post processing algorithms could greatly reduce execution times but could highly increase the risk of appearance of hallucinations.[25]

Evaluation on simulated data showed a similar beam-hardening correction to that of *FDK+2DCalBH* and *FDK+JS* for high dose data, while also reducing the low-sampling artifacts present in low-dose studies, as the method proposed by Elbakri et al.[14] and our previous statistical method, *1DIterBH*. The better approximation of the beam-hardening function provides a lower RMSE with respect to the true-density values compared to *1DIterBH* in all tissues. Errors in adipose tissue were larger than those in soft tissue for all the methods, probably due to the assumption of a negligible difference in

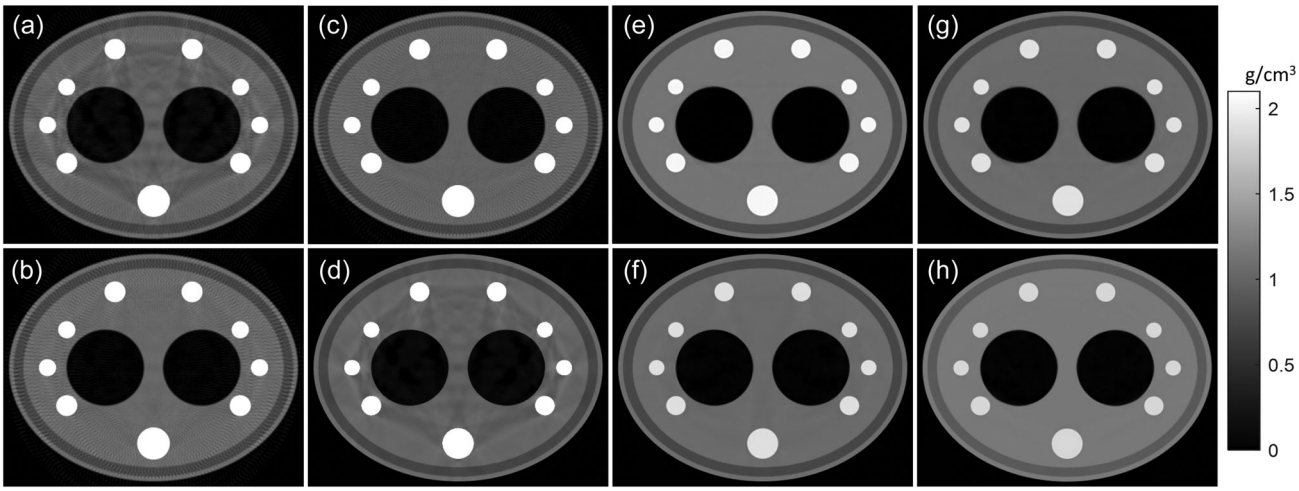

FIGURE 3 Phantom in the standard-dose scenario reconstructed with *FBP* (a) *FBP+JS* (b), *FBP+2DCalBH* (c), *PWLS* (d), *SegFreePoly* (e), *1DiterBH* (f) and *2DIterBH* method calibrated with ideal (g) and realistic (h) phantom.

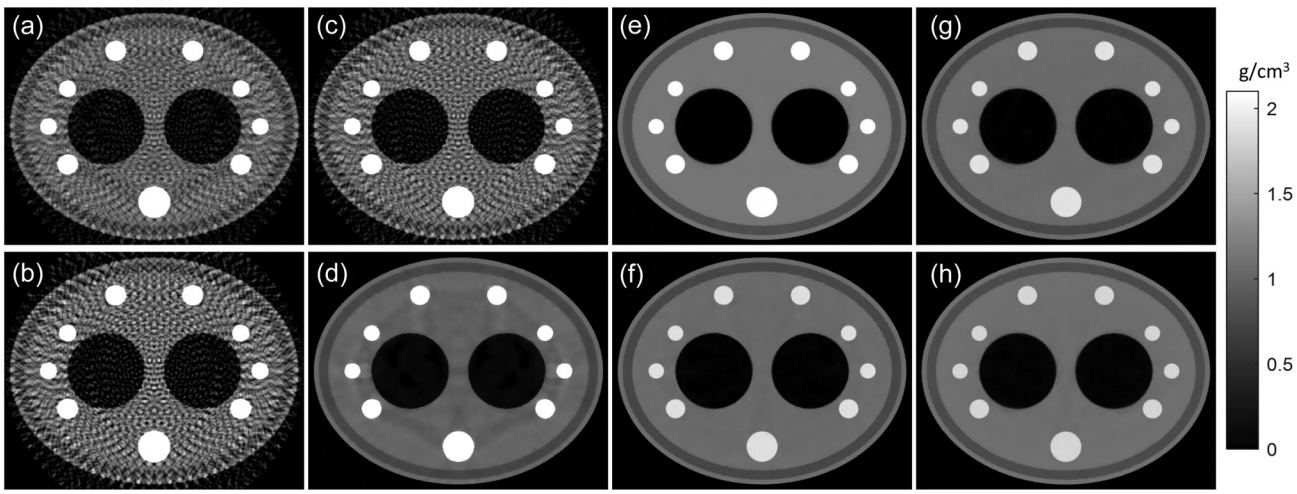

FIGURE 4 Phantom in the ultra-low-dose scenario reconstructed with *FBP* (a) *FBP+JS* (b), *FBP+2DCalBH* (c), *PWLS* (d), *SegFreePoly* (e), *1DiterBH* (f) and *2DIterBH* method calibrated with ideal (g) and realistic (h) phantom.

the attenuation properties of soft and adipose tissue. Using the realistic phantom resulted in a higher error in soft tissue and bone, probably due to a mismatch in the attenuation properties of the phantom materials and the tissues. This could be solved by correcting the mass thickness of PMMA and AL with their effective mass attenuation coefficients, obtained experimentally from the beam-hardening function as in.[10] Although the errors were higher in soft tissue, the realistic phantom resulted in a much lower error in adipose tissue. Future work will explore if a different soft-tissue equivalent material, like water, could provide a compromise between both tissue types.

Since our method currently models the object as being composed of two materials, further investigation is needed for scans involving metallic implants. The method could be extended to a third material such as titanium. Given its difference in density (4.50 g/cm^3) with respect to bone, there will not be overlap in the tissue fractions. The major challenge would be the design of a three-material phantom to properly span the BH function in the three axes. An alternative to the three-material phantom could be to modulate the third dimension with a heuristic function to account for the extra material, similarly to what is done in.[15] Other materials such as iodine contrast agents would require further study, given the low difference in density between iodinated and non-contrast blood.

Evaluation on 3D real data showed similar results to those obtained in simulated data for the slice used to find the optimum parameters. Nevertheless, the improvement on the model used both in *FDK+2DCalBH* and the proposed method provides a more robust correction than *1DIterBH* and *JS*, assuring a dark band elimination over the whole sample, independently of the bone distribution. The method proposed by Elbakri

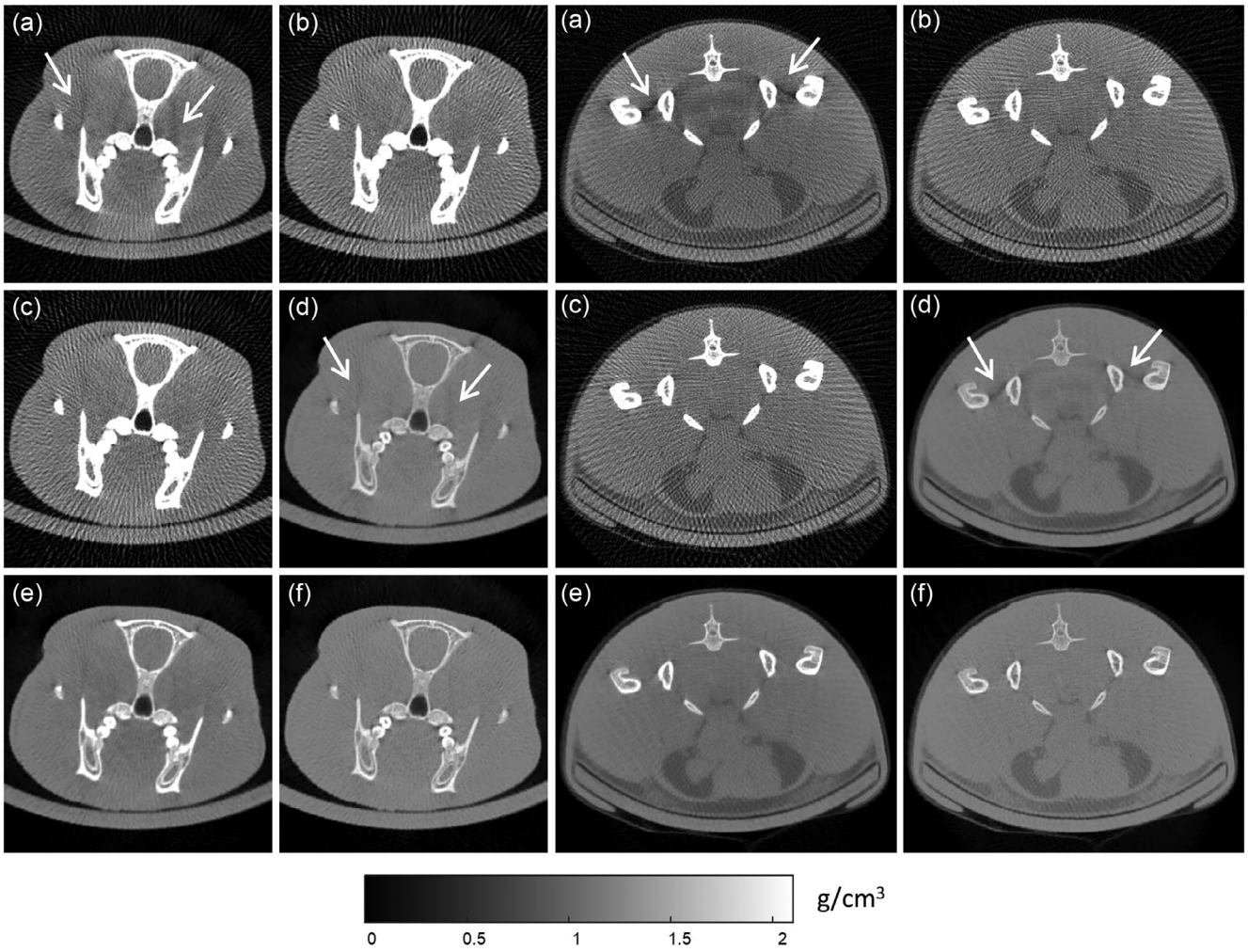

FIGURE 5 Axial slices of two rodent studies used to calibrate the FDK+JS and the simplified statistical reconstruction methods, reconstructed with uncorrected *FDK* (a), *FDK+JS* (b), *FDK+2DCalBH* (c), *SegFreePoly* (d), *1DIterBH* (e) and the *2DIterBH* (f). White arrows indicate dark-band artifacts.

et al.[14] corrected the low sampling artifacts, but did not fully compensate the dark bands, showing the need of the knowledge of the full spectrum for this method.

The reduction of streaks because of the noise model and the penalty term is not a novel result. In this regard, we used a simple noise model that does not reflect the complete physics of the CT acquisition. Future work could evaluate the possibility of including a more accurate noise model, for example, considering the measurements as a sum of energy-scaled Poisson processes, each with a different scale factor. However, the main point of our work is the reduction of the beam-hardening artifacts in low-dose studies with no need for heuristic parameters that would depend on the quantity of tissue traversed.

The streaks produced by low sampling in non-iterative methods may have similar values than bone and, thus, will be included in the bone mask,[15] reducing the effectiveness of the methods. In *2DCalBH*, such segmentation errors hinder the selection of the appropriate linearization functions, leading to inconsistent projection data and an increase of all the values considered as bone, which will exacerbate the streak artifacts. The proposed model overcomes such limitation by estimating the attenuation at each voxel based on piecewise density-dependent tissue fractions, which are updated at each iteration and therefore avoids possible segmentation problems in low-dose studies. The selection of the intervals for the density-dependent tissue fractions was based on the typical densities for soft-tissue and cortical bone found in NIST. Further evaluation of the effect of the definition of these intervals on the recovered density values is warranted.

The proposed method does not consider spatially dependent energy fields such as those produced by beam modulating filters. The effect of these filters could be added to the estimation of bone mass

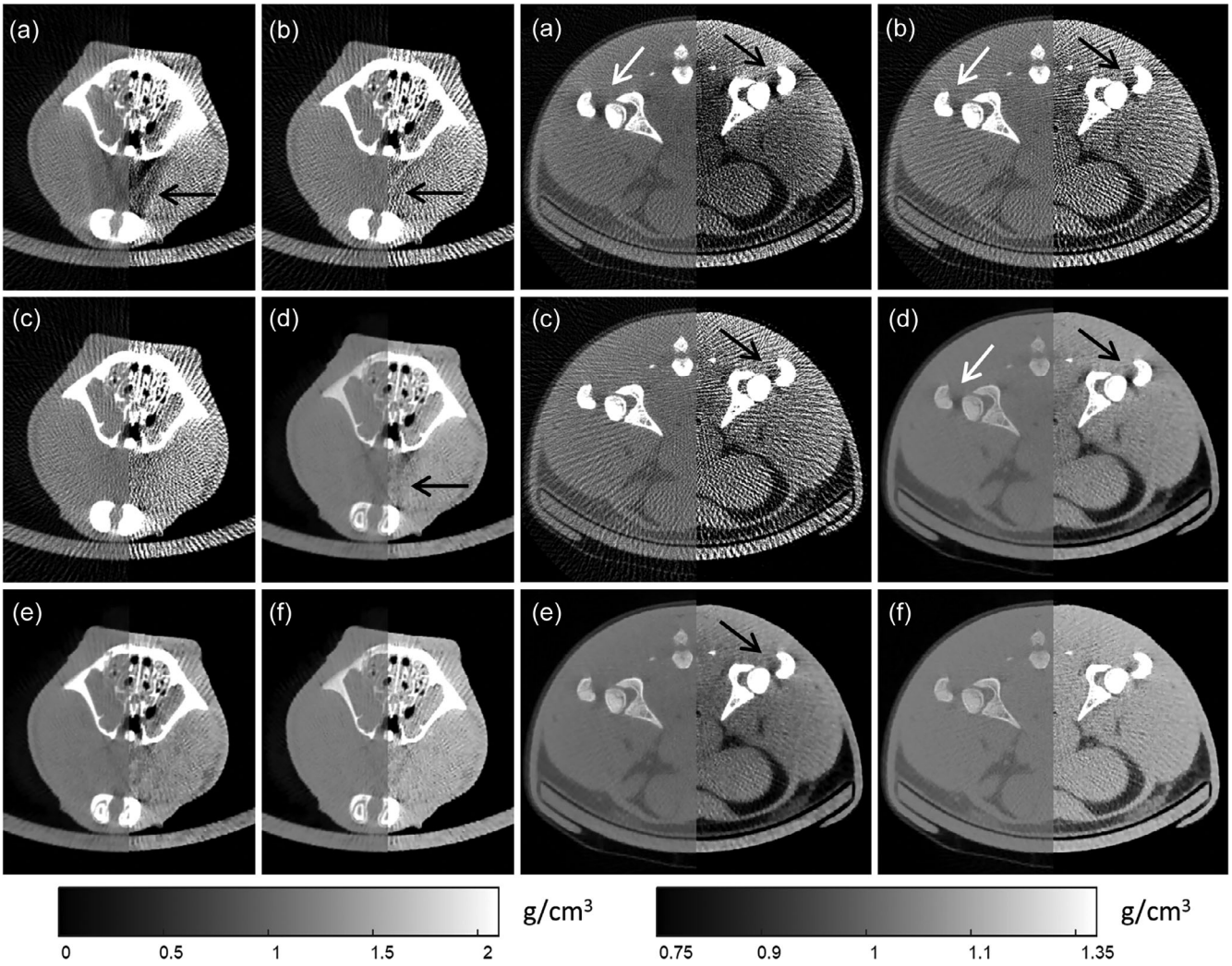

FIGURE 6 A different axial slice of each of the two rodent studies reconstructed with uncorrected *FDK* (a), *FDK+JS* (b), *FDK+2DCalBH* (c), *SegFreePoly* (d), *1DIterBH* (e) and the *2DIterBH* (f). Arrows indicate dark-band artifacts. Color bars corresponding to each image half are shown at the bottom.

thickness on a ray-by-ray basis, given that we know the aluminum equivalent thickness of the filter for each ray.

Although the focus of this work is small-animal scenarios, future work will explore the possibility of using the proposed method in clinical scenarios. To this end, we will need to evaluate if the same equivalent materials are valid to emulate the attenuation properties with a size equivalent to the human body thicknesses at the clinical energies. Also, the scatter effect will have to be evaluated as it is more important in clinical studies than in preclinical studies and may lead to an overestimation of the beam hardening effect during the calibration process. Nevertheless, this problem might be mitigated by the fact that the majority of diagnostic helical CT systems incorporate antiscatter grids which, combined with scatter correction methods, could effectively suppress the scatter effect.

Using an empirical model for the beam-hardening effect, obtained through calibration, in an iterative reconstruction method enables a robust correction of beam hardening artifacts in low dose studies, independently of the bone distribution. The incorporation of this method into a real small animal CT scanner is straightforward, when raw sinogram values are available, only needing a minor modification of the standard calibration step available in most commercial scanners.

ACKNOWLEDGMENTS

This work was supported by Ministerio de Ciencia e Innovación, Agencia Estatal de Investigación (AEI/10.13039/501100011033): PID2019-110369RB-I00 (RADHOR); PID2021-128862OB-I00, co-funded by 'ERDF A way of making Europe'; PDC2021-121656-I00 (MULTIRAD), co-funded by the European Union

'NextGenerationEU'/PRTR. Also funded by Instituto de Salud Carlos III through the projects PMPTA22/00121 and PMPTA22/00118, co-funded by the European Union 'NextGenerationEU'/MRR. And by the ASPIDE Project funded by the European Union's Horizon 2020 Research and Innovation Programme under grant 801091. The CNIC is supported by Instituto de Salud Carlos III, Ministerio de Ciencia e Innovación, and the Pro CNIC Foundation.

CONFLICT OF INTEREST STATEMENT

The authors declare no conflicts of interest.

DATA AVAILABILITY STATEMENT

Results for all methods as well as the projection data from the rodent studies and the calibration phantom are available at https://zenodo.org/records/7840374.

REFERENCES

1. Barrett JF, Keat N. Artifacts in CT: recognition and avoidance. *Radiographics*. 2004;24(6):1679-1691.
2. Brooks RA, Di Chiro G. Beam hardening in x-ray reconstructive tomography. *Phys Med Biol*. 1976;21(3):390-398.
3. Herman GT. Correction for beam hardening in computed tomography. *Phys Med Biol*. 1979;24(1):81.
4. Joseph PM, Spital RD. A method for correcting bone induced artifacts in computed tomography scanners. *J Comput Assist Tomogr*. 1978;2(1):100-108.
5. Kyriakou Y, Meyer E, Prell D, Kachelrieß M. Empirical beam hardening correction (EBHC) for CT. *Med Phys*. 2010;37(10):5179-5187.
6. Schüller S, Sawall S, Stannigel K, et al. Segmentation-free empirical beam hardening correction for CT. *Med Phys*. 2015;42(2):794-803.
7. Jin P, Bouman CA, Sauer KD. A model-based image reconstruction algorithm with simultaneous beam hardening correction for X-ray CT. *IEEE Trans Comput Imag*. 2015;1(3):200-216.
8. Würfl T, Hoffmann M, Aichert A, Maier AK, Maaß N, Dennerlein F. Calibration-free beam hardening reduction in x-ray CBCT using the epipolar consistency condition and physical constraints. *Med Phys*. 2019;46(12):e810-e822.
9. Würfl T. Anwendungen von Datenkonsistenzbedingungen in der Kegelstrahl-Computertomographie. *Applications of Data Consistency Conditions in Cone-Beam Computed Tomography*; 2020.
10. Martinez C, Fessler JA, Desco M, Abella M. Simple beam-hardening correction method (2DCalBH) based on 2D linearization. *Phys Med Biol*. 2022;67(11):115005.
11. Yan CH, Whalen RT, Beaupre GS, Yen SY, Napel S. Reconstruction algorithm for polychromatic CT imaging: application to beam hardening correction. *IEEE Trans Med Imaging*. 2000;19(1):1-11.
12. De Man B, Nuyts J, Dupont P, Marchal G, Suetens P. An iterative maximum-likelihood polychromatic algorithm for CT. *IEEE Trans Med Imaging*. 2001;20(10):999-1008.
13. Elbakri IA, Fessler JA. Statistical image reconstruction for polyenergetic X-ray computed tomography. *IEEE Trans Med Imaging*. 2002;21(2):89-99.
14. Elbakri IA, Fessler JA. Segmentation-free statistical image reconstruction for polyenergetic X-ray computed tomography with experimental validation. *Phys Med Biol*. 2003;48(15):2453.
15. Abella M, Martinez C, Desco M, Vaquero JJ, Fessler JA. Simplified statistical image reconstruction for X-ray CT with beam-hardening artifact compensation. *IEEE Trans Med Imaging*. 2020;39(1):111-118.
16. Martinez C, Fessler JA, Desco M, Abella M, Segmentation-free statistical method for polyenergetic X-ray computed tomography with a calibration step. In *Proc. 6th Int. Conf. Image Formation X-Ray Computed Tomography*. 2020; 118-121.
17. Vaquero JJ, Redondo S, Lage E, et al. Assessment of a new high-performance small-animal X-ray tomograph. *IEEE Trans Nucl Sci*. 2008;55(3):898-905.
18. Erdogan H, Fessler JA. Monotonic algorithms for transmission tomography. *IEEE Trans Med Imaging*. 1999;18(9):801-814.
19. Hubbell JH, Seltzer SM, *Tables of X-ray mass attenuation coefficients and mass energy-absorption coefficients 1 keV to 20 MeV for elements Z = 1 to 92 and 48 additional substances of dosimetric interest*. 1995; Accessed March 26 2024 http://physics.nist.gov/PhysRefData/XrayMassCoef/cover.html
20. Huber PJ. In: Sons JW, ed. *Robust Statistics*. 1981.
21. Fessler JA. Penalized weighted least-squares image reconstruction for positron emission tomography. *IEEE Trans Med Imaging*. 1994;13:290-300.
22. Hudson HM, Larkin RS. Accelerated image reconstruction using ordered subsets of projection data. *IEEE Trans Med Imaging*. 1994;13(4):601-609.
23. Abella M, Serrano E, Garcia- Blas J, et al. FUX-Sim: implementation of a fast universal simulation/reconstruction framework for X-ray systems. *PLoS ONE*. 2017;12(7):e0180363.
24. Martinez C, Martinez C, de Molina C, Desco M, Abella M. Optimization of a calibration phantom for quantitative radiography. *Med Phys*. 2020;48(3):1039-1053.
25. Bhadra S, Kelkar VA, Brooks FJ, Anastasio MA. On hallucinations in tomography image reconstruction. *Trans Med Imaging*. 2021;40(11):3249-3260.

How to cite this article: Sanderson D, Martinez C, Fessler JA, Desco M, Abella M. Statistical image reconstruction with beam-hardening compensation for X-ray CT by a calibration step (2DIterBH). *Med Phys*. 2024;1-10. https://doi.org/10.1002/mp.17239